

Scanning inverse fluorescence correlation spectroscopy

Jan Bergstrand,¹ Daniel Rönnlund,¹ Jerker Widengren,¹ and Stefan Wennmalm^{2,*}

¹Department of Applied Physics, Albanova University Center, Royal Institute of Technology-KTH, 106 91 Stockholm, Sweden

²Science for Life Laboratory, Department of Applied Physics, Royal Institute of Technology-KTH, 171 65 Solna, Sweden

*stewen@kth.se

Abstract: Scanning Inverse Fluorescence Correlation Spectroscopy (siFCS) is introduced to determine the absolute size of nanodomains on surfaces. We describe here equations for obtaining the domain size from cross- and auto-correlation functions, measurement simulations which enabled testing of these equations, and measurements on model surfaces mimicking membranes containing nanodomains. Using a confocal microscope of 270 nm resolution the size of 250 nm domains were estimated by siFCS to 257 ± 12 nm diameter, and 40 nm domains were estimated to 65 ± 26 nm diameter. Applications of siFCS for sizing of nanodomains and protein clusters in cell membranes are discussed.

© 2014 Optical Society of America

OCIS codes: (180.2520) Fluorescence microscopy; (180.5810) Scanning microscopy; (300.6280) Spectroscopy, fluorescence and luminescence.

References and links

1. S. C. Prinster, C. Hague, and R. A. Hall, "Heterodimerization of G protein-coupled receptors: specificity and functional significance," *Pharmacol. Rev.* **57**(3), 289–298 (2005).
2. I. Bethani, S. S. Skånland, I. Dikic, and A. Acker-Palmer, "Spatial organization of transmembrane receptor signalling," *EMBO J.* **29**(16), 2677–2688 (2010).
3. D. Lingwood and K. Simons, "Lipid Rafts As a Membrane-Organizing Principle," *Science* **327**(5961), 46–50 (2010).
4. S. W. Hell and J. Wichmann, "Breaking the Diffraction Resolution Limit by Stimulated Emission: Stimulated-Emission-Depletion Fluorescence Microscopy," *Opt. Lett.* **19**(11), 780–782 (1994).
5. M. J. Rust, M. Bates, and X. W. Zhuang, "Sub-diffraction-limit imaging by stochastic optical reconstruction microscopy (STORM)," *Nat. Methods* **3**(10), 793–795 (2006).
6. M. Heilemann, S. van de Linde, M. Schüttelz, R. Kasper, B. Seefeldt, A. Mukherjee, P. Tinnefeld, and M. Sauer, "Subdiffraction-resolution fluorescence imaging with conventional fluorescent probes," *Angew. Chem. Int. Ed. Engl.* **47**(33), 6172–6176 (2008).
7. E. Betzig, G. H. Patterson, R. Sougrat, O. W. Lindwasser, S. Olenych, J. S. Bonifacino, M. W. Davidson, J. Lippincott-Schwartz, and H. F. Hess, "Imaging intracellular fluorescent proteins at nanometer resolution," *Science* **313**(5793), 1642–1645 (2006).
8. V. Westphal, S. O. Rizzoli, M. A. Lauterbach, D. Kamin, R. Jahn, and S. W. Hell, "Video-rate far-field optical nanoscopy dissects synaptic vesicle movement," *Science* **320**(5873), 246–249 (2008).
9. C. Eggeling, C. Ringemann, R. Medda, G. Schwarzmann, K. Sandhoff, S. Polyakova, V. N. Belov, B. Hein, C. von Middendorff, A. Schönle, and S. W. Hell, "Direct observation of the nanoscale dynamics of membrane lipids in a living cell," *Nature* **457**(7233), 1159–1162 (2009).
10. D. Magde, W. W. Webb, and E. Elson, "Thermodynamic Fluctuations in a Reacting System - Measurement by Fluorescence Correlation Spectroscopy," *Phys. Rev. Lett.* **29**(11), 705–708 (1972).
11. R. Rigler, U. Mets, J. Widengren, and P. Kask, "Fluorescence Correlation Spectroscopy with High Count Rate and Low-Background - Analysis of Translational Diffusion," *Eur Biophys J Biophys* **22**(3), 169–175 (1993).
12. J. Widengren and R. Rigler, "Fluorescence correlation spectroscopy as a tool to investigate chemical reactions in solutions and on cell surfaces," *Cell. Mol. Biol. (Noisy-le-grand)* **44**(5), 857–879 (1998).
13. S. Wennmalm, P. Thyberg, L. Xu, and J. Widengren, "Inverse-fluorescence correlation spectroscopy," *Anal. Chem.* **81**(22), 9209–9215 (2009).
14. S. Wennmalm and J. Widengren, "Inverse-fluorescence cross-correlation spectroscopy," *Anal. Chem.* **82**(13), 5646–5651 (2010).

15. S. Wennmalm and J. Widengren, "Inverse-fluorescence correlation spectroscopy: more information and less labeling," *Front Biosci (Schol Ed)* **3**(1), 385–392 (2011).
 16. E. Elson, Washington University, St Louis, Missouri, USA, (personal communication, 2013).
 17. T. Sandén, R. Wyss, C. Santschi, G. Hassaine, C. Deluz, O. J. Martin, S. Wennmalm, and H. Vogel, "A zeptoliter volume meter for analysis of single protein molecules," *Nano Lett.* **12**(1), 370–375 (2012).
 18. D. Wildanger, E. Rittweger, L. Kastrup, and S. W. Hell, "STED microscopy with a supercontinuum laser source," *Opt. Express* **16**(13), 9614–9621 (2008).
 19. D. Rönnlund, Y. Yang, H. Blom, G. Auer, and J. Widengren, "Fluorescence Nanoscopy of Platelets Resolves Platelet-State Specific Storage, Release and Uptake of Proteins, Opening up Future Diagnostic Applications," *Adv Healthc Mater* **1**(6), 707–713 (2012).
 20. S. Costantino, J. W. D. Comeau, D. L. Kolin, and P. W. Wiseman, "Accuracy and dynamic range of spatial image correlation and cross-correlation spectroscopy," *Biophys. J.* **89**(2), 1251–1260 (2005).
 21. N. O. Petersen, P. L. Höddelius, P. W. Wiseman, O. Seger, and K. E. Magnusson, "Quantitation of Membrane Receptor Distributions by Image Correlation Spectroscopy: Concept and Application," *Biophys. J.* **65**(3), 1135–1146 (1993).
 22. D. L. Kolin and P. W. Wiseman, "Advances in image correlation spectroscopy: Measuring number densities, aggregation states, and dynamics of fluorescently labeled macromolecules in cells," *Cell Biochem. Biophys.* **49**(3), 141–164 (2007).
 23. A. Honigsmann, G. van den Bogaart, E. Iraheta, H. J. Risselada, D. Milovanovic, V. Mueller, S. Müller, U. Diederichsen, D. Fasshauer, H. Grubmüller, S. W. Hell, C. Eggeling, K. Kühnel, and R. Jahn, "Phosphatidylinositol 4,5-bisphosphate clusters act as molecular beacons for vesicle recruitment," *Nat. Struct. Mol. Biol.* **20**(6), 679–686 (2013).
 24. F. Göttfert, C. A. Wurm, V. Mueller, S. Berning, V. C. Cordes, A. Honigsmann, and S. W. Hell, "Coaligned Dual-Channel STED Nanoscopy and Molecular Diffusion Analysis at 20 nm Resolution," *Biophys. J.* **105**(1), L01–L03 (2013).
 25. B. Hein, K. I. Willig, C. A. Wurm, V. Westphal, S. Jakobs, and S. W. Hell, "Stimulated Emission Depletion Nanoscopy of Living Cells Using SNAP-Tag Fusion Proteins," *Biophys. J.* **98**(1), 158–163 (2010).
-

1. Introduction

The plasma membrane is the site of a large number of molecular interactions crucial for the survival of the cell [1]. Cell surface receptors transmit signals across the membrane and are often drug targets, such as in the case of G-protein coupled receptors which are the target of about 30-40% of all pharmaceutical drugs. As part of their normal function receptors often cluster into oligomers [2] which can be as large as 100 nm in diameter, but exist likely in all sizes down to dimers smaller than 5 nm diameter. Receptor clustering may occur inside so called lipid rafts which consist of glycosphingolipids and transmembrane proteins, commonly believed to be 10-100 nm in diameter [3].

Receptor clustering and lipid rafts are difficult to study because their sizes are below the diffraction limit of visible light. Confocal laser scanning microscopes (LSMs) have a resolution of about 250-300 nm and can thus only determine the size of clusters and domains larger than that. Analysis of those of smaller size has to rely on fluorescence intensity which is an uncertain approach due to effects such as fluorescence quenching, non-uniform illumination, and bleaching.

The super-resolution techniques (STED [4], PALM/STORM [5–7]) which have emerged strongly during the last ten years allow the generation of fluorescence images with a resolution down to about 20-50 nm. This opens up for analysis of cluster- and raft-sizes that are inaccessible to confocal imaging, and especially the localization techniques are suitable for detection of clusters. Still, a cluster determined to be no larger than 30 nm diameter may contain anywhere from one to 50 monomers.

Moreover, reports on super-resolution analysis of fast dynamics are so far limited to STED-imaging of a 2x2 μm area of the cell with a temporal resolution of 35 ms [8]. Dynamics in the μs time range of nanodomains in living cells have been analyzed by STED-FCS by varying the diameter of the detection area, however absolute sizes of domains cannot be measured [9].

Fluorescence Correlation Spectroscopy (FCS) [10] has during the last 20 years developed into an established technique for analyzing molecular interactions in solution and on the surface and inside of living cells [11]. FCS analyzes concentrations and sizes of particles and

biomolecules at typically nanomolar concentrations, and sizes are estimated indirectly from the diffusion coefficient [12]. Recently, Inverse Fluorescence Correlation Spectroscopy (iFCS) was introduced which instead analyses particles by detecting a signal from the solution in which the particles are dissolved [13]. In iFCS the volume of particles is determined directly from the amount of displaced fluorophores, in contrast to the indirect estimation from the diffusion coefficient. It thus gives an absolute value of the particle size, and has in addition the potential to be more sensitive since the amplitude of the iFCS curve is proportional to the square of the particle volume, while the diffusion time in standard FCS scales with the cubic root of the particle mass.

iFCS was originally demonstrated on a standard FCS instrument on unlabeled particles of sizes down to 100 nm diameter dissolved in a concentrated dye solution [13]. The variant iFCCS analyzes instead labeled particles, and their absolute volume is determined by cross-correlating the signal from the labeled particles with that from the surrounding solution [14]. The volume of particles is in iFCCS given by the amplitude of the anti-correlation curve, and it has an advantage of allowing the labeled particles to be analyzed specifically even in the presence of other, non-labeled particles.

Performing iFCS on a cell membrane is attractive due to the amount of fundamental interactions that take place there. The possibility to determine the absolute size of receptor clusters before and after stimulation of the same living cell would be highly valuable and is currently not feasible. Furthermore, the iFCS technique itself would benefit from a two dimensional surface compared to 3D solution, since a larger fraction of the signal is displaced in a 2D situation [15]. Recently such analyses have been performed using iFCS by Elliot Elson and associates for analyzing the size of nanodomains in giant unilamellar vesicles (GUVs) [16].

When iFCS has been applied to 3D diffusion in solution, particles 600 times smaller than the detection volume have been detected, in a diffraction limited focus [13] as well as for protein molecules in nano-wells [17]. Assuming that the same sensitivity can be achieved on a surface, sizing of 20-25 nm diameter objects by a confocal microscope should be possible, and 3-4 nm diameter objects using a STED microscope of 40 nm FWHM.

Here, Scanning Inverse FCS (siFCS) is introduced to analyze immobile surfaces. Surfaces mimicking fixed cell membranes are used consisting of a single layer of densely packed fluorescent NPs on a glass coverslip. The majority of NPs are green fluorescent and mimic labeled phospholipids, and a few NPs are red fluorescent and mimic the protein clusters or nanodomains whose size are to be determined. The fixed surfaces are scanned using a confocal or a STED-microscope. Analysis using siFCS indicates that sizing is possible of membrane objects with a diameter at least seven times smaller than the resolution of the microscope used.

2. Materials and methods

2.1 Sample preparation

Fluorescent carboxylated nanoparticles (NPs) with excitation/emission spectrum of 580/605 ("green NPs") or 625/605 ("red NPs") were purchased from Life Technologies. The green NPs had a diameter of either 200 nm or 36 nm and the red NPs a diameter of either 250 nm or 40 nm. Coverslips (22 × 22 mm and 0.13-0.16 mm thick) and microscope slides (26 × 76 mm and 1-1.2 mm thick) were purchased from Menzel-Gläser. A single layer of NPs was formed by first coating the coverslip with Poly-L-lysine (PLL, Sigma Aldrich) which resulted in a positively charged surface, followed by incubation of the negatively charged carboxylated NPs.

For the 200/250 nm NPs, the PLL-coating was generated by first cleaning the cover slip with a solution of 70% ethanol and 1% HCl, then draining in ultra-pure water and drying with nitrogen. 100 μ l of PLL diluted 1:10 in ultra-pure water was incubated for 5 minutes and then

washed in ultra-pure water. The cover slips were left to dry at room temperature overnight. The stock solutions of the 250 nm NPs were diluted as follows: For the incubation of NPs onto the PLL-coated coverslips, green and red NPs were mixed in PBS buffer pH 7.3 such that 80% of the NPs were green and 20% were red. 100 μ l of this NP mixture was let to incubate on the PLL-coated cover slips for 20 minutes, followed by washing richly but gently with carbonate buffer pH 8.3 (4.2g NaCHO₃, MW = 84.01, was dissolved in 1 L dH₂O and adjusted to pH 8.3 through pipetting with HCl) to remove any additional layers of NPs. The cover slips were then air dried at room temperature for about 2 hours. Finally the cover slips were mounted onto a microscope slide using 15 μ l of Mowiol mounting medium.

For coupling of the 40 nm NPs cover slips were sonicated for 15 minutes in 2-propanol, then washed in ultra-pure water and blow dried with nitrogen, then 100 μ l of PLL was incubated for 5 minutes followed by washing in ultra-pure water and air drying at room temperature over-night. The NPs were mixed in PBS pH 7.3 such that 90% of the NPs were green and 10% were red. Because the 40 nm NPs were more likely to aggregate the NP mixture was sonicated for 20 minutes before incubation on the PLL-coated coverslips for 30 minutes. Thereafter the cover slips were washed with a pipette with carbonate buffer of pH 8.4, followed by air drying at room temperature for 2 hours. Finally the cover slips were mounted onto a microscope slide using 15 μ l Mowiol mounting medium.

2.2 Microscope

The microscope used for confocal as well as STED images was a homebuilt two-colour laser scanning STED (Stimulated Emission Depletion) microscope, the design of which has been described in detail previously [18, 19]. For confocal imaging the resolution of the microscope was 260-280 nm FWHM, while for STED imaging the resolution was about 40 nm FWHM.

2.3 Simulations

In order to be able to investigate the effect of parameters such as NP density, crosstalk, noise, and microscope resolution, similar surfaces as those prepared were simulated. A custom written MATLAB code was used for the simulations. Two images were generated, corresponding to the red and the green images, by randomly distributing a given number of dots in each image. To simulate NPs with a physical size each dot was given a radius, for example six pixels, which limited how close neighboring NPs could be positioned. In this way no NPs overlapped physically in the green or in the red image. This corresponded to a single layer of NPs on the cover slip. Each dot was then given a normalized Gaussian intensity profile where the full width half maximum (FWHM) of the profile corresponded to the resolution of the microscope in the red and the green channels respectively. A number of parameters could thereby be adjusted freely: image size, NP sizes, number of red and green NPs, and the resolution in the red and the green channel. In order to simulate cross talk which in the actual measurements was present even after cross-talk compensation (see section 4.2 Experiments), a fraction of the intensity in the green image was added to the red image and vice versa. By denoting the intensity in the green image I_{green} and the intensity in the red image I_{red} , the intensity in the red image including crosstalk, called $I_{\text{red+CT}}$ is given by

$$I_{\text{red+CT}} = I_{\text{red}} + f I_{\text{green}} \quad (1)$$

where f is the fraction of the signal in the green channel that is detected also in the red channel. For crosstalk in the green image the equation is the same but with the red and green subscripts switched. We estimated about 1% crosstalk in our measurements even after cross-talk compensation and therefore the simulations including crosstalk were carried out using $f=0.005$ or $f=0.01$.

Noise was included by adding the absolute value of normally distributed random numbers to each pixel in each image. The noise was then tuned by scaling the standard deviation σ of

the normal distribution. In this study $\sigma = 0.2$ which means that the background signal was slightly less than 20% of the intensity of a single NP since this intensity was scaled to 1. Based on a visual comparison of the simulated and the real images, this was likely a somewhat higher noise level than in the real case. This way of implementing noise does not include the Poisson distributed photon noise which is proportional to the square root of the intensity value at each pixel [20]. However if the noise can be assumed to be uncorrelated it should not enter into the correlation functions except in the dominator in Eq. (3) and Eq. (4). Only considering uncorrelated background noise should therefore be at least a quantitative indication of how noise influences the sizing.

2.4 Data analysis

Data analysis was carried out using MATLAB. Cross- and auto-correlation curves were most quickly generated by a two dimensional fast Fourier transform (Eq. (7)). The two-dimensional correlation functions were projected onto the x- and y-plane and averaged over the projections. In this way the correlation functions were plotted as one dimensional curves which facilitates reading of the amplitudes $G_{CC}(0)$ and $G_{AC,r}(0)$, and furthermore it is computationally faster to perform a one dimensional Gaussian fit.

The number of red NPs in each image had to be counted in order to estimate the NP density. For this a MATLAB code was written which detected intensities in the image above a given cut-off value and then checked whether that intensity value corresponded to a NP or not. This MATLAB program counted the number of NPs with an accuracy of about 95%, and as a routine control a few images were in addition counted manually.

In order to reduce crosstalk the microscope uses time-gated excitation and detection meaning that the green and red excitation laser pulses are separated in time by 40 ns. The initial green excitation pulse excites the green fluorophores but also some of the red fluorophores. A fraction of the light from the red fluorophores will be detected by the green detector (this constitutes the crosstalk in the green channel), but most of it will be recorded by the red detector. In this way a cross-talk image of the crosstalk in the green channel is created by the red detector. 40 ns later a red excitation pulse will excite mostly the red fluorophores but also some of the green fluorophores. A fraction of the light from the green fluorophores will be detected by the red detector (this constitutes the crosstalk in the red channel), but most of it will be recorded by the green detector. In this way a cross-talk image of the crosstalk in the red channel is created by the green detector (Fig. 1).

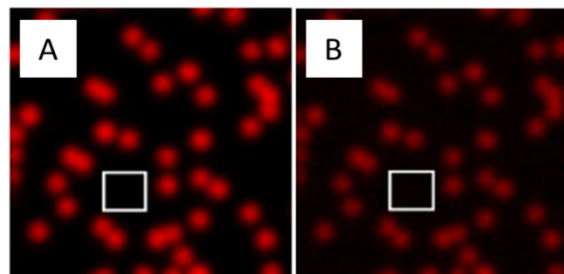


Fig. 1. A typical image of red NPs (A) and the corresponding cross-talk image (B). The white square marks an area where the average intensity is compared between the images. For this particular area the mean intensity in the original image (A) was $I_r \approx 5$ counts and the mean intensity in the cross-talk image (B) was $I_{CT} \approx 15$ counts giving $F \approx 0.3$.

To compensate for crosstalk in both directions, a fraction F of the entire cross-talk image I_{CT} was subtracted from the original image I_{orig} . This fraction was estimated by taking the average intensity I_r (in the case of the red image) of a dark area in the original image divided by the average intensity I_{CT} of the same area in the corresponding cross-talk image. Thereby $F = I_r/I_{CT}$ and the intensity of the cross-talk reduced image becomes

$$I_{reduced} = I_{orig} - F \times I_{CT}. \quad (2)$$

The value of F turned out to be approximately 0.3 for the green as well as for the red images, and for confocal and STED images. Note that this does not imply that the crosstalk is 30%, but that the cross-talk image records about 3 times more of the crosstalk than the actual image.

3. Theory

We assumed that the ergodic principle holds in the sense that scanning over an immobilized surface is equivalent to particles passing through a detection volume. Furthermore the particles should be uniformly and randomly distributed on the surface so that the number of particles within the detection area is Poisson distributed [21]. With these two assumptions the theory of iFCCS was directly applied to scanned surfaces. When performing iFCCS on diffusing particles it is the time dependent cross-correlation function that is analyzed, where the amplitude of the cross-correlation function reveals information about the volume of the diffusing particles. However when iFCCS is performed on a surface it is rather the two dimensional spatial cross-correlation function $G_{CC}(x, y)$ that should be considered, defined as

$$G_{CC}(x, y) = \frac{\langle \delta i_r(x'+x, y'+y) \delta i_g(x', y') \rangle}{\langle i_r(x', y') \rangle \langle i_g(x', y') \rangle} \quad (3)$$

where $i_r(x', y')$, $i_g(x', y')$ is the red and the green intensity respectively at a point (x', y') on the surface and $\delta i(x', y') = i(x', y') - \langle i \rangle$ is the fluctuation of the intensity around its mean value and $\langle \dots \rangle$ is the spatial average taken by integrating over all the points (x', y') .

The autocorrelation function for the red image $G_{AC,r}(x, y)$ was also considered. It is defined in the same way as $G_{CC}(x, y)$ but with $g = r$ and thus becomes

$$G_{AC,r}(x, y) = \frac{\langle \delta i_r(x'+x, y'+y) \delta i_r(x', y') \rangle}{\langle i_r(x', y') \rangle \langle i_r(x', y') \rangle}. \quad (4)$$

When referring to properties that are shared by the cross-correlation function and the autocorrelation function they will just be called the correlation functions $G(x, y)$. If the intensity of the detection area is assumed to have a Gaussian intensity profile, then $G_{CC}(x, y)$ and $G_{AC,r}(x, y)$ should be fitted with a Gaussian function [20–22] given by

$$G_{fit}(x, y) = G(0) e^{-\frac{x^2+y^2}{\sigma}} + G_{\infty} \quad (5)$$

where $G(0)$, σ and G_{∞} are the fitting parameters. The offset G_{∞} was included since when obtaining the correlation function the data was restricted by the scanned area and the sampling intervals and enough data was not sampled for the correlation functions to go to zero [21]. The parameter σ is the e^{-2} -decay which defines the radius of the detection area.

When an image was recorded by the microscope it was represented by a matrix $i(k, l)$, $k, l = 1, 2, \dots, N$ where N is the total number of samplings intervals along the x and y-dimension, i.e. it was assumed to be a square image. Each element in this matrix represents a pixel where the value of a pixel at point (k, l) is the intensity at that point. For this discrete set of intensities the spatial average is given by summing over all pixels and then dividing by the number of pixels so the discrete correlation function at point (k, l) becomes

$$G(k, l) = \frac{\frac{1}{(N-k)(N-l)} \sum_{m=1}^{N-k} \sum_{n=1}^{N-l} \delta i_s(m+k, n+l) \delta i_t(n, m)}{\frac{1}{N^2} \sum_{n=1, m=1}^N i_s(m, n) \frac{1}{N^2} \sum_{n=1, m=1}^N i_t(m, n)} \quad (6)$$

where $s = r$, $t = g$ for the cross-correlation function and $s = t = r$ for the autocorrelation function. This way of calculating the correlation functions numerically was implemented directly in MATLAB. However, obtaining the correlation functions by a Fourier transform made the computations considerably faster. The correlation function is then given by

$$G(k, l) = \frac{N^2 F^{-1} \left[F[i_s(m, n)] \cdot F^* [i_t(m, n)] \right]}{\sum_{n=1, m=1}^N i_s(m, n) \sum_{n=1, m=1}^N i_t(m, n)} \quad (7)$$

where F^{-1} is the inverse Fourier transform and $*$ denotes the complex conjugate. The amplitude $G_{CC}(0)$ is the parameter that will be of the greatest interest for iFCCS since it gives the projected area of the particles on the surface [15], however also the amplitude $G_{AC,r}$ is needed. To see how $G_{CC}(0)$ depends on the projected particle area, consider a red particle that is fully within the green detection focus area A_g . It occupies an area A_p and reduces thereby the green intensity by a factor A_p/A_g where A_g is the area of the green detection focus, and the expression for the mean value of the green intensity becomes

$$\langle i_g \rangle = I_g = I_{g,tot} \left(1 - \frac{A_p}{A_g} N_{pg} \right) + I_{g,CT} \quad (8)$$

and the mean value of the red intensity becomes

$$\langle i_r \rangle = I_r = Q_p N_{pr} + I_{r,CT} \quad (9)$$

where $I_{g,tot}$ is the total green intensity that would be detected if there were no red particles on the surface, N_{pr} and N_{pg} are the average numbers of red particles in the red and the green detection areas respectively and Q_p is the intensity of each red particle. The last terms in each equation, $I_{g,CT}$ and $I_{r,CT}$, are the cross-talk terms that come from that a fraction of the red signal leaks over into the green channel and vice versa.

By assuming zero crosstalk and using that $\langle \delta i_r \delta i_g \rangle = \Delta I_r \Delta I_g$ where ΔI is the standard deviation of the Poisson distributed intensity fluctuations from particles within the detection area so that $\Delta N_{ps} = \sqrt{N_{ps}}$ ($s = r, g$), it follows that

$$\langle \delta i_r \delta i_g \rangle = \Delta \left(I_{g,tot} \left(1 - \frac{A_p}{A_g} N_{pg} \right) \right) \cdot \Delta (Q_p N_{pr}) = -I_{g,tot} \frac{A_p}{A_g} Q_p \sqrt{N_{pg} N_{pr}} \quad (10)$$

Together with Eq. (8) and Eq. (9) and inserting it into the definition of $G_{CC}(x, y)$ (Eq. (3)) for $(x, y) = 0$ gives the theoretical expression for the amplitude of the cross-correlation function for the ideal case of zero crosstalk

$$G_{CC}(0) = \frac{-I_{g,tot} \frac{A_p}{A_g} Q_p \sqrt{N_{pg} N_{pr}}}{Q_p N_{pr} \left(I_{g,tot} \left(1 - \frac{A_p}{A_g} N_{pg} \right) \right)} = \frac{-A_p}{\sqrt{A_g A_r} \left(1 - \frac{A_p}{A_g} N_{pg} \right)} \quad (11)$$

where in the last step the identity $N_{pr}/N_{pg} = A_r/A_g$ was used. The fact that the amplitude is negative indicates anti-correlation between the green and red channels.

If the particle size is much smaller than the detection focus area A_g and the particle density n is low so that $N_{pg} = n A_g < 1$, then $(A_p/A_g) N_{pg} = n A_p \ll 1$ and the amplitude can be approximated by

$$G_{CC}(0) \approx \frac{-A_p}{\sqrt{A_g A_r}} \quad (12)$$

which is a useful equation for estimating the particle size when the particle density cannot be determined exactly. These are the basic equations used to determine the particle size.

The detection focus area may be difficult to define exactly, since it may be defined by the e^{-2} -width or the e^{-1} -width or by some other definition. Regarding the density of particles, it may in principle be determined by simply calculating the number of particles in the image, which is possible given that the separation of the particles is on average greater than the resolution of the microscope. In this study the particles were always countable and the red detection focus area A_r could therefore be estimated from the amplitude of the autocorrelation function for only the red image. For the red images the average number of particles N_{pr} in the red detection area was given by [21]

$$N_{pr} = \frac{1}{G_{AC,r}(0)} \quad (13)$$

where $G_{AC,r}(0)$ is the amplitude of the autocorrelation function for the red image. At the same time N_{pr} was given by

$$N_{pr} = \frac{A_r N_p}{A} = A_r n \quad (14)$$

where A is the area of the surface scanned by the microscope, N_p is the total number of particles in the red image and n is the total density of particles in the red image. Together Eqs. (13) and 14 give

$$A_r = \frac{1}{n G_{ac,r}(0)}. \quad (15)$$

Therefore by determining $G_{AC,r}(0)$ and counting the number of particles in the red image the red detection area A_r could be estimated, without knowledge of the particle size. With this estimate of A_r , the green detection area A_g could also be estimated by assuming that the intensities in the foci of the red and green lasers were distributed in the same way and that A_g was defined by the same cut-off as A_r for some decay width, e.g. the full width at half maximum (FWHM) or the e^{-2} width. If some of these decay widths were known for both channels, here called ω_r respectively ω_g , then

$$A_g = \left(\frac{\omega_g}{\omega_r}\right)^2 \cdot A_r = \left(\frac{\omega_g}{\omega_r}\right)^2 \frac{1}{n G_{ac,r}(0)}. \quad (16)$$

By inserting the expressions for A_r and A_g into Eq. (11) and solving for A_p the final equation for determining the projected particle area becomes

$$A_p = \frac{1}{n} \frac{\omega_g}{\omega_r} \left[-\frac{G_{ac,r}(0)}{G_{CC}(0)} + \frac{\omega_g}{\omega_r} \right]^{-1} \quad (17)$$

(note that the area will be positive since $G_{CC}(0) < 0$). To use this equation the widths of the foci must be known for both the red and green lasers. For this study two types of imaging were used, confocal and STED, where the width was given by the FWHM of the foci (i.e. the resolution). For the confocal imaging it was $\omega_r = 280$ nm and $\omega_g = 260$ nm and for STED $\omega_r = \omega_g = 40$ nm. Insertion of these values into Eq. (17) and using that the particles are circular

such that the diameter is given by $d = \sqrt{4A_p/\pi}$, gave the expression for the size of spots in confocal images

$$d = \frac{2}{\sqrt{\pi}} \sqrt{\frac{1}{n} \frac{13}{14}} \left[-\frac{G_{ac,r}(0)}{G_{CC}(0)} + \frac{13}{14} \right]^{-\frac{1}{2}} \quad (18)$$

and in STED images

$$d = \frac{2}{\sqrt{\pi}} \sqrt{\frac{1}{n}} \left[-\frac{G_{ac,r}(0)}{G_{CC}(0)} + 1 \right]^{-\frac{1}{2}}. \quad (19)$$

These equations were used for determining the size of spots on the surface, which in our case were the fluorescent NPs. For this the amplitudes of the cross-correlation function and the auto-correlation function and the density of NPs needed to be known, which all could be obtained experimentally. Note that these equations were derived assuming zero crosstalk, and it was therefore important to reduce crosstalk as much as possible in the experiments and to take crosstalk into account in the subsequent analysis.

4. Results

4.1 Simulations

The $5 \times 5 \mu\text{m}$ simulated images consisted of either 100×100 pixels corresponding to a step length (the distance the laser focus moves between data collection points) of 50 nm as for confocal images, or they consisted of 250×250 pixels corresponding to a step length of 20 nm as for the STED images. The resolution of the confocal microscope of about 270 nm was simulated using a Gaussian intensity profile with FWHM of 6 pixels (equaling 300 nm in the confocal case), while the STED resolution of 40 nm turned out to be most realistically simulated using a Gaussian intensity profile with a FWHM of 4 pixels (corresponding to 80 nm, Fig. 2). With one pixel equaling 50 nm in the confocal images, a bead size of 40 nm could not be simulated and instead the smallest simulated bead size was 50 nm.

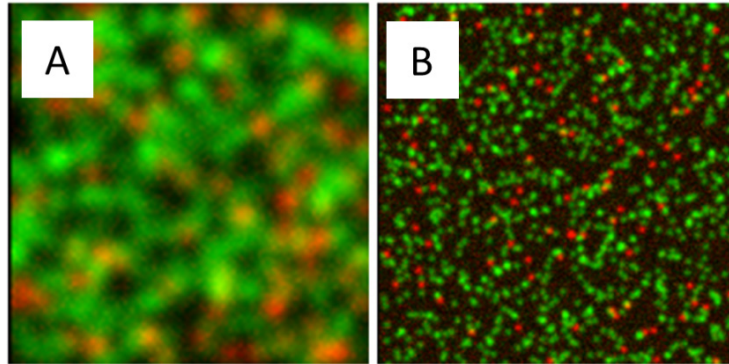


Fig. 2. Simulated images, including noise, with 100 and 1000 red and green NPs respectively. (A) Simulated confocal image of size 100×100 pixels, NP size was 1 pixel and the resolution was 6 pixels. This corresponds roughly to confocal imaging of 40 nm NPs (compare with Fig. 9(A)). (B) Simulated STED image. The location of the NPs is not the same as in Fig. 2(A). Image size was 250×250 pixels, NP size was 1 pixel and the resolution was 4 pixels. This corresponds roughly to STED imaging of the 40 nm NPs (compare with Fig. 9(B)).

Table 1 displays simulations where the number of red NPs was kept constant at 50 and the number of green NPs was varied, and three different NP sizes were simulated. The simulations indicate that as long as $> 10\%$ of the surface is covered by green NPs, the NP size estimated from $G_{CC}(0)$ has a standard deviation not exceeding $\sim 30\%$, even when realistic

levels of noise and crosstalk were included. However, the NP size was overestimated at low total concentrations which is likely an effect of the increased gap between NPs.

Table 1. Simulations of Confocal Images with Varying Densities of Green NPs

Percentage of total area covered by NPs (# green NPs)	NP size (pixels)	Estimated size w/o crosstalk and noise (pixels)	Estimated size with crosstalk and noise (pixels)
5% (590)	1	1.7 ± 0.7 (54)	1.7 ± 0.7 (12)
10% (90)	3	3.4 ± 1.1 (84)	3.0 ± 1.0 (66)
20% (50)	5	5.4 ± 0.8 (99)	4.5 ± 1.0 (97)
40% (150)	5	5.4 ± 0.5 (100)	5.3 ± 0.5 (100)
80% (360)	5	4.9 ± 0.3 (100)	5.5 ± 0.3 (100)

The resolution was 6 pixels corresponding to a confocal microscope, for images of size 100×100 pixels with a total of 50 red NPs in each image. 100 images were generated for each simulation. The crosstalk was 1%. The error is the standard deviation. The value in parenthesis after the size estimate is the total number of images yielding a cross-correlation curve with negative amplitude used for the size estimation.

For small NP sizes, another effect at low total concentrations was that the cross-correlation curves sometimes had positive amplitude, even when no noise or crosstalk was added to the images. A likely explanation for this effect is that in those cases the intensity profiles of the red and the green NPs overlap to the extent that the net result was a positive correlation. This issue will be further investigated below. If only curves with negative amplitude were taken into account when calculating the average $G_{CC}(x)$ the obtained sizes from using Eq. (17) were reasonable and within the standard deviation, however, if all curves were used then the amplitude was reduced (Fig. 3).

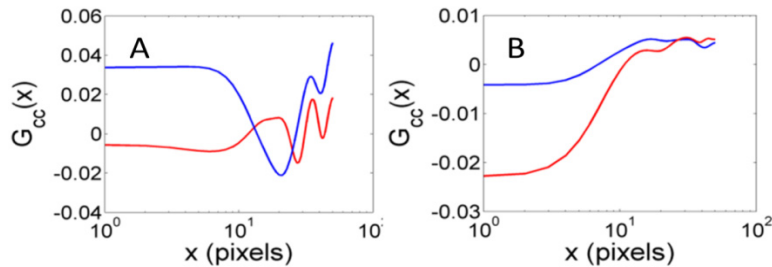


Fig. 3. Cross-correlation curves for simulated images containing 100×100 pixels. The NP size was 1 pixel and the number of red and green NPs was 100 and 1000 respectively. The resolution was 6 pixels. (A) Examples of single-image cross-correlation curves. A curve with positive amplitude (blue) and a curve with negative amplitude (red) are shown. (B) Average correlation curves for 100 images: of all cross-correlation curves (blue), and of all cross-correlation curves with negative amplitude, 53 in total.

For the simulated confocal images, the phenomenon of cross-correlation curves with positive amplitude was most frequently observed when the NP size was 1 pixel (46 out of 100 images, Table 1), corresponding to a NP size of 50 nm. In order to investigate this phenomenon further, a second series of images were simulated at different concentrations of green NPs, using a fixed NP size of 50 nm, confocal and also STED images, with or without crosstalk and noise.

For the images without crosstalk and noise, a lower concentration of green NPs resulted in a higher chance of a positive cross-correlation amplitude (Table 2). This was possibly because the increased variance of the cross-correlation curves at lower concentrations resulted in a larger fraction of curves with positive amplitude. Again, lower concentrations of green NPs resulted in over estimation of the (red) NP size. Summarizing the estimations without crosstalk and noise, sizing of the 50 nm NPs was satisfactory when the concentrations of green NPs was above 1000 NPs per $5 \times 5 \mu\text{m}$ area.

In the simulations including crosstalk and noise, 1% crosstalk was added to the confocal images and 0.5% to the STED images (Table 3). A value of 1% crosstalk in the STED images was also tested but resulted in no anti-correlation at all. The addition of crosstalk increased the number of positive cross-correlation amplitudes, as expected since crosstalk appearing in the red image correlates positively with the original green image, and vice versa for crosstalk from the red to the green image. This resulted in fewer images yielding anti-correlation and a reduced average cross-correlation amplitude. As a result of this cross-talk effect, lowering the concentration of green NPs resulted in fewer cross-correlation curves with positive amplitude, i.e. the opposite of the situation with no crosstalk (Table 2). Thus, when crosstalk and noise were added, the NPs were over estimated at low concentrations of green NPs and under estimated at high concentrations of green NPs. This emphasizes the importance of minimizing crosstalk during imaging and compensating for crosstalk in the analysis.

Table 2. Simulations of 50 nm Diameter NPs, without Crosstalk and Noise

# Green NPs	NP size	Estimated size Confocal	Estimated size STED
100	1	2.2 ± 0.9 (51)	2.0 ± 0.8 (61)
300	1	1.7 ± 0.7 (53)	1.7 ± 0.7 (77)
1000	1	1.3 ± 0.5 (52)	1.3 ± 0.5 (76)
3000	1	1.0 ± 0.4 (55)	1.2 ± 0.4 (84)
9000	1	1.0 ± 0.3 (60)	1.1 ± 0.2 (96)

Table 3. Simulations of 50 nm Diameter NPs, with Crosstalk and Noise Added

# Green NPs	NP size	Estimated size Confocal	Estimated size STED
100	1	2.1 ± 0.8 (44)	2.6 ± 1.1 (36)
300	1	1.6 ± 0.8 (42)	2.1 ± 0.7 (28)
1000	1	1.2 ± 0.4 (34)	1.8 ± 1.0 (19)
3000	1	0.9 ± 0.5 (19)	1.4 ± 0.6 (10)
9000	1	0.6 ± 0.4 (8)	-

For Table 2 and 3, the simulations included 100 red NPs in each image. Each simulation generated 100 images and the error is the standard deviation. The value in parenthesis following the estimated size is the number of images yielding cross-correlation curves with negative amplitude used for the size estimation. Table 2: Confocal simulations were performed with image size 100×100 pixels and resolution 6 pixels. STED simulations were performed with image size 250×250 pixels and resolution 4 pixels. Table 3: The crosstalk was 1% for the confocal simulations and 0.5% for the STED simulations. For 9000 green NPs no STED images resulted in anti-correlation. The noise was set to about 20% of the intensity per NP.

As mentioned earlier the likely explanation for the positive cross-correlation amplitudes in images without crosstalk or noise is the overlap between the intensity profiles of the red and the green NPs (Fig. 4). This was supported by the fact that the number of cross-correlation curves yielding anti-correlation was higher for the STED simulations, where the intensity profile was narrower, than for the confocal simulations (Table 2).

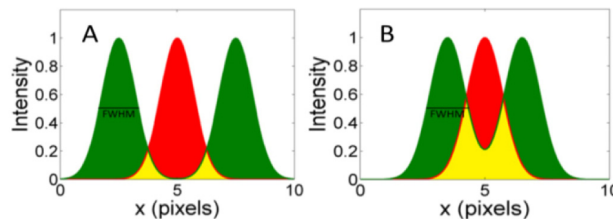


Fig. 4. The intensity profiles of two green NPs surrounding a red NP. The yellow areas indicate the overlap of the intensity profiles which may contribute positively to the cross-correlation amplitude. (A) Small overlap of the intensity profiles. (B) Large overlap of the intensity profiles.

To further confirm this hypothesis a fourth series of simulations of 50 nm NPs was performed, without crosstalk and noise, with a resolution varying from a FWHM of 2 to 12 pixels, with 100 simulations for each resolution (Table 4). As expected, when the FWHM of the NPs increased the number of positive cross-correlation amplitudes increased.

Table 4. Simulations of 50 nm NPs without Crosstalk and Noise, with Varying Resolution

Width (FWHM) (pixels)	# Images yielding anti-correlation	NP size (pixels)	Estimated size (pixels)
2	99	1	1.1 ± 0.3
4	69	1	1.1 ± 0.4
6	52	1	1.3 ± 0.5
8	46	1	1.4 ± 0.6
10	24	1	1.3 ± 0.5
12	16	1	1.4 ± 0.7

The image size was 100×100 pixels. The number of red and green NPs was 100 and 1000 respectively. 100 images were generated for each simulation. The error is the standard deviation.

4.2. Experiments

4.2.1 250 nm NPs

A total of 14 confocal and STED images were recorded for the 250 nm NPs (Fig. 5). An intensity trace of a confocal image shows how the red peaks coincide with the green dips (Fig. 5(C)). The resolution of the STED-microscope, about 40 nm in lateral direction, was sufficient to resolve individual 250 nm NPs (Fig. 5). Multiple layers of NPs were rarely seen and could easily be identified in STED-images (Fig. 5(B), arrow).

The theoretical expression for the amplitude of the cross-correlation curve (Eq. (11)) indicates that the presence of a red NP in the detection area reduces the green signal in proportion to the projected area of the NP. However, red 250 nm NPs are larger than the detection area of the STED-focus and therefore siFCS-analysis of the 250 nm NPs was only performed using the confocal images.

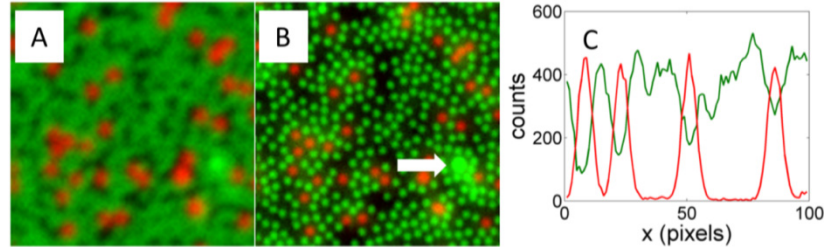


Fig. 5. Typical confocal (A) and STED image (B) of the same scanned area on the cover slip. The size of the scanned area was $5 \times 5 \mu\text{m}$. The white arrow points out an area on the surface where the NPs most likely had formed a multiple layer, which however had little effect on the analysis. (C) Trace for arbitrary line in the confocal image.

The red and green images were cross-correlated to obtain $G_{CC}(0)$ and the red image was auto-correlated to obtain $G_{AC,r}(0)$ (Fig. 6). By counting the red NPs in each image the density of red NPs was estimated to be $n = 1.97 \pm 0.32 \times 10^{-6}$ NPs/nm², where the error is the standard deviation. This gave all the parameters needed in Eq. (17) to estimate the diameter d of the red NPs. The NPs covered about 60% of the surface and therefore comparison with the simulations (Table 1) indicates that all images should yield anti-correlation. This was also observed.

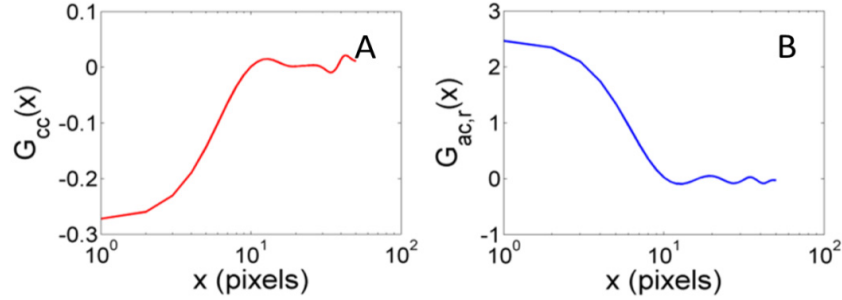


Fig. 6. Typical cross correlation curve (A) and auto-correlation (B) curves for a single image of the 200 nm NPs. On the x-axis 1 pixel corresponds to 50 nm.

The individual cross- and auto-correlation curves from all images were averaged and fitted to Eq. (5) (Fig. 7). The Gaussian fit yielded the amplitudes $G_{CC}(0) = -0.22$ and $G_{AC,r}(0) = 1.95$. Both fits also yielded the same e^{-2} -decay widths of 267 nm. Using this as the radius of the detection area [20] resulted, according to Eq. (13), in the density 2.3×10^{-6} NPs/nm² which differs by only 15% to the density 1.97×10^{-6} NPs/nm² obtained by counting. Thus the crosstalk present has only a minor effect on the size estimation. Inserting these values for the amplitudes and the mean density of 1.96×10^{-6} NPs/nm² into Eq. (18) gave an average diameter of the red NPs of $d = 246$ nm, close to the specified value 250 nm.

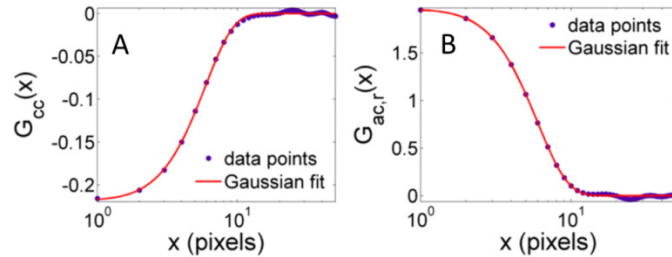


Fig. 7. Average cross- (A) and auto correlation (B) curves for all 14 raw images of the 250 nm NPs. The Gaussian fit of the data points gave the amplitudes $G_{CC}(0) = -0.22$ and $G_{AC,r}(0) = 1.95$. The decay width at e^{-2} was 267 nm for both curves. On the x-axis 1 pixel corresponds to 50 nm.

If the size was instead estimated from each individual image followed by averaging over all estimates, then $d = 248 \pm 17$ nm where the error is the standard deviation.

Next we investigated the effect of compensating for crosstalk as described in the data analysis section above (Fig. 8). Following this procedure and estimating the diameter of the NPs from each image after reducing for crosstalk and averaging gave

$$d = 257 \pm 12 \text{ nm.}$$

The specified value is still within the standard deviation, which is now slightly smaller (5%). Averaging instead all correlation curves for the cross-talk reduced images (Fig. 8) yielded $G_{CC}(0) = -0.27$ and $G_{AC,r}(0) = 2.15$ which gave the size $d = 259$ nm using $n = 1.97 \times 10^{-6}$ NPs/nm². The e^{-2} -decay width was 270 nm for both curves which is about the same as for the raw images. Estimating the radius of the detection area from the e^{-2} -decay width together with $G_{AC,r}(0) = 2.15$ and Eq. (13) gave the density as 2.0×10^{-6} NPs/nm² for the red NPs.

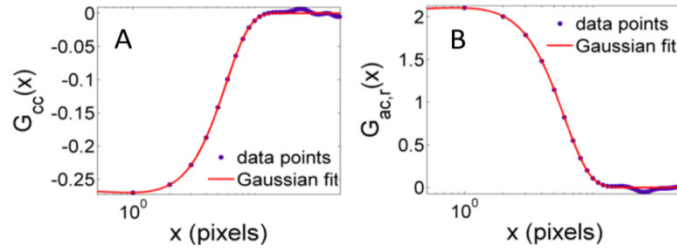


Fig. 8. Average cross- (A) and auto-correlation (B) curves for all 14 cross-talk reduced images of the 250 nm NPs. The amplitudes were $G_{CC}(0) = -0.27$ and $G_{AC,r}(0) = 2.15$ and the decay widths at e^{-2} was 270 nm for both curves. On the x-axis 1 pixel corresponds to 50 nm.

Multiplying together the density with the area of the red NPs gave $n \cdot A_p = 1.97 \times 10^6 \cdot \pi \cdot 125^2 = 0.01$, indicating that 1% of the area was covered by red NPs. Since $n \cdot A_p \ll 1$ it is interesting to test the approximation given by Eq. (12). Using the values of $G_{CC}(0)$ and the e^{-2} -decay width = 270 nm as the radius for the detection area gave an approximation of the diameter for raw and cross-talk reduced images respectively of

$$d = \frac{2}{\sqrt{\pi}} \sqrt{(13/14) \cdot \pi \cdot 270^2 \cdot 0.22} = 244 \text{ nm} \quad (\text{raw})$$

$$d = \frac{2}{\sqrt{\pi}} \sqrt{(13/14) \cdot \pi \cdot 270^2 \cdot 0.27} = 270 \text{ nm} \quad (\text{cross-talk reduced})$$

which are good estimations for the NP size.

Finally, deconvolution by a built in function in MATLAB (deconvlucy) which uses the Richardson-Lucy algorithm was tested. Applying this onto the images and performing the size estimation gave $d = 250 \pm 17$ nm.

4.2.2 40 nm NPs

The 40 nm diameter NPs are equally large or slightly smaller than the detection area of the STED microscope, and siFCS analysis could therefore be performed using confocal microscopy as well as STED microscopy. The 40 nm sample had about 1000 green NPs and 100 red NPs in a scanned area of $5 \times 5 \mu\text{m}$, indicating that only about 10% of the area was covered by NPs (Fig. 9). However, the earlier described simulations for these sizes and densities indicated that size estimation should still be possible though a slight overestimation may occur due to the low concentration.

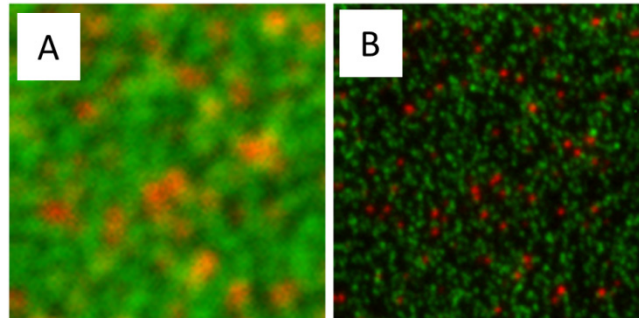


Fig. 9. Typical confocal (A) and STED (B) images of the same $5 \times 5 \mu\text{m}$ area of 40 nm NPs. In the confocal image the individual NPs cannot be resolved because of the resolution of ~ 270 nm (compare with Fig. 5(A)). For the STED image the ~ 40 nm resolution can almost distinguish individual NPs.

A total of 42 images were recorded. From the raw images 19 of the cross-correlation curves had negative amplitude, for the confocal as well as for the STED images (negative cross-correlation amplitudes were not necessarily obtained from the same confocal and STED images). By only considering those images that yielded a negative cross-correlation amplitude, estimating the size from each individual image and then averaging gave for the confocal images $d = 63 \pm 25$ nm and for the STED images $d = 43 \pm 8$ nm. The STED images thus gave a better estimate and a smaller standard deviation which could be a result of the higher resolution of the STED microscope. Still, for the confocal estimate the specified size was within the standard deviation.

Averaging all the anti-correlation amplitudes and the corresponding auto-correlation amplitudes gave the mean amplitudes for confocal images $G_{CC}(0) = -0.0079$ and $G_{AC,r}(0) = 0.4631$ (Fig. 10). The e^{-2} -decay width for the cross-correlation curve was 410 nm and that for the autocorrelation curve 290 nm. Counting the red NPs in each image gave a density $n = 4.16 \pm 0.37 \times 10^{-6}$ nm $^{-2}$ (std). Using these values together with Eq. (17) gave the estimated NP size $d = 69$ nm for the raw confocal images.

From the STED images the amplitudes were $G_{CC}(0) = -0.013$ and $G_{AC,r}(0) = 1.98$, and the e^{-2} -decay widths were 145 nm and 170 nm for the cross- and the auto-correlation curves respectively (Fig. 10). Using these values together with the density 4.16×10^{-6} nm $^{-2}$ gave the estimated NP size $d = 45$ nm for raw STED images.

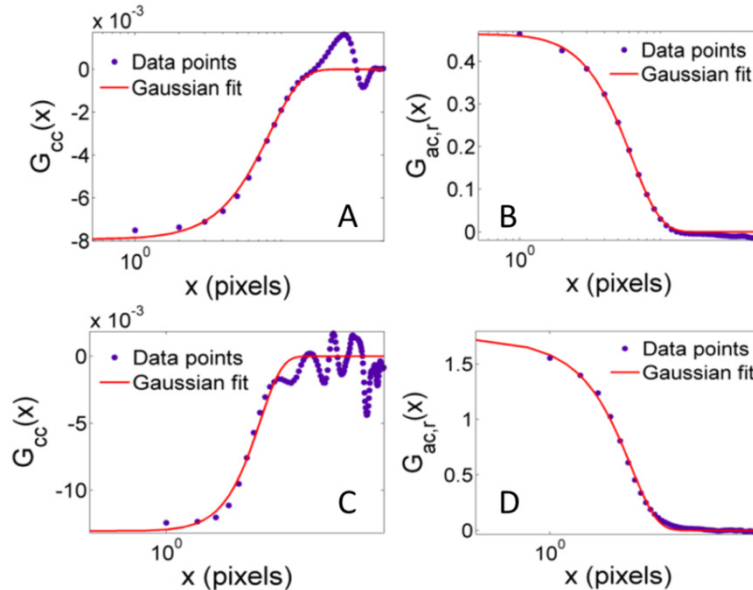


Fig. 10. (A) and (B): Average cross- and auto-correlation curves for all raw confocal images yielding anti-correlation, 19 out of 42, of the 40 nm NPs. The amplitudes were $G_{CC}(0) = -0.08$ and $G_{AC,r}(0) = 0.46$. The decay widths at e^{-2} were 410 nm 290 nm for the cross- and the auto-correlation curves respectively. On the x-axis 1 pixel corresponds to 50 nm. (C) and (D): Average curves from the 19 out of 42 STED images that yielded anti-correlation. The amplitudes were $G_{CC}(0) = -0.013$ and $G_{AC,r}(0) = 1.98$. The decay widths at e^{-2} were 156 nm and 170 nm for the cross- and the auto-correlation curves respectively. On the x-axis 1 pixel corresponds to 20 nm.

Compensation for crosstalk was attempted for the 40 nm NPs as well, using the same approach as for the 250 nm NPs (Fig. 11). This resulted in anti-correlation for 29 of the confocal images and 38 of the STED images out of the total 42. Estimating the size of the red NPs from each individual image and then averaging gave for the confocal images

$$d = 65 \pm 26 \text{ nm}$$

and for the STED images

$$d = 76 \pm 17 \text{ nm.}$$

For the STED images the size estimation deviates more from the specified 40 nm than the estimate from the raw STED images, but on the other hand the Gaussian fit of the average curves (Fig. 12) was somewhat better when crosstalk was taken into account. The overestimation of the NP size was expected since the NPs are not packed densely enough. The fact that the STED images yield a larger overestimation is likely explained by the fact that while the presence of crosstalk reduces the size-estimates, the presence of noise increases the size estimates. In addition, STED-siFCS was more sensitive to crosstalk as well as noise than confocal-siFCS, which can be seen by comparing Table 2 and 3. Since the recorded images were compensated for crosstalk but not for noise, the higher sensitivity of STED-siFCS to noise likely resulted in a larger over-estimation compared to confocal-siFCS.

The amplitudes of the average confocal cross-talk reduced curves were $G_{CC}(0) = -0.013$ and $G_{AC,r}(0) = 0.73$ and the e^{-2} -decay widths were 335 nm and 290 nm for the cross- and the auto-correlation curves respectively (Fig. 13(A, B)), which yielded $d = 69$ nm from the cross-talk-compensated confocal images. For the STED images the corresponding amplitudes were $G_{CC}(0) = -0.12$ and $G_{AC,r}(0) = 1.98$ and the decay widths at e^{-2} were 156 nm and 154 nm for the cross- and auto-correlation curves respectively (Fig. 12), which yielded $d = 75$ nm.

For comparison, the cross-correlation functions for cross-talk compensated confocal images of the 250 nm and 40 nm NPs are shown in the same graph (Fig. 11(C)). The cross-correlation amplitudes scale with the square of the NP diameter and the amplitudes differ here by a factor of ~ 20 , in line with the respective estimated diameters of 257 nm and 65 nm.

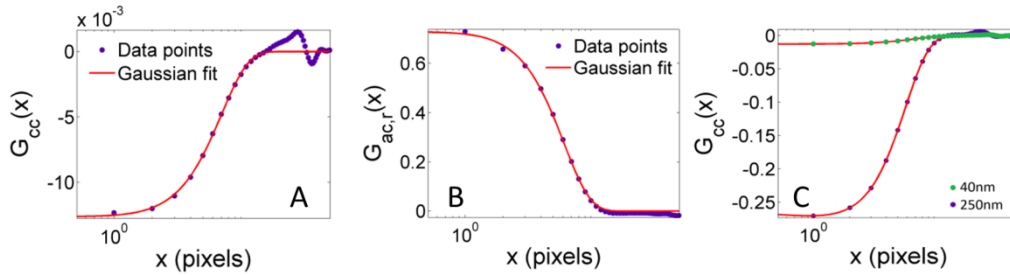


Fig. 11. Average cross-correlation curve of the cross-talk compensated confocal images of 40 nm NPs yielding negative amplitude (A) and the corresponding auto-correlation curve (B). For comparison the average cross-correlation curves from confocal images of the 40 nm NPs and the 250 nm NPs are displayed in the same graph (C). On the x-axis 1 pixel corresponds to 50 nm.

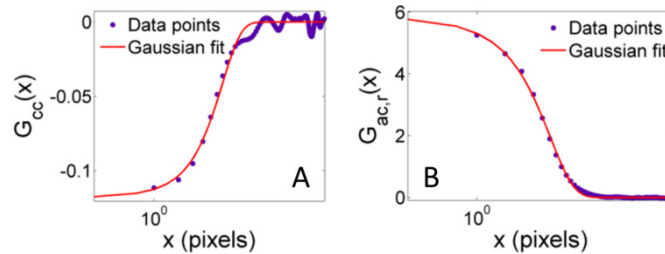


Fig. 12. Average cross-correlation curve of the cross-talk compensated STED images yielding negative amplitude, 38 out of 42 (A), and the corresponding auto-correlation curve (B). The amplitudes were $G_{CC}(0) = -0.12$ and $G_{AC,r}(0) = 6.46$. The decay widths at e^{-2} were 156 nm and 154 nm for the cross- and the auto-correlation curves respectively. On the x-axis 1 pixel corresponds to 20 nm.

In order to possibly further improve the cross-talk reduced images they were deconvoluted with the Richardson-Lucy algorithm. In the subsequent cross-correlation analysis 26 of the

confocal images and 40 of the STED images yielded anti-correlation out of the total 42 images. A larger number of anti-correlated curves was expected since the positive cross-correlation amplitudes are a result of overlap between the red and green intensity profiles, and the width of the intensity profiles are reduced by deconvolution. Thus the statistics should be somewhat better for the deconvoluted images than for the raw data.

The result of the size estimation was

$$d = 51 \pm 19 \text{ nm (Confocal, cross – talk compensated and deconvoluted)}$$

and

$$d = 59 \pm 17 \text{ nm (STED, cross – talk compensated and deconvoluted)}.$$

The estimates were closer to the specified values which were within the standard deviation, and the relative standard deviations were about the same (~50%). Averaging over all the anti-correlation curves and over the corresponding auto-correlation curves resulted for the confocal images in $G_{CC}(0) = -0.029$ and $G_{AC,r}(0) = 1.78$ which yielded a diameter of 68 nm. The e^{-2} -decay widths for the confocal curves were 173 nm and 200 nm for the cross- and auto-correlation curves respectively. For the STED images the amplitudes were $G_{CC}(0) = -0.38$ and $G_{AC,r}(0) = 26.8$ which yielded a diameter of 65 nm. This auto-correlation amplitude was about five times higher than that of the non-deconvoluted auto-correlation curve. This could result if NPs that are less bright disappeared due to the deconvolution, leaving a strongly reduced apparent concentration. Furthermore the detection area was reduced since the effective resolution was enhanced, as can be seen from the e^{-2} -decay widths of 69 nm and 65 nm respectively.

Since $n \cdot A_p = 4.16 \times 10^{-6} \text{ nm}^{-2} \cdot \pi \cdot 20^2 \text{ nm}^2 = 0.005 \ll 1$, the approximation of Eq. (12) was tested for size-estimation. Using $G_{CC}(0) = -0.013$ for confocal and $G_{CC}(0) = -0.12$ for STED from the cross-talk reduced images and using the e^{-2} -decay widths ~290 nm and ~150 nm for the confocal and STED detection areas respectively [20] yielded

$$d \approx \frac{2}{\sqrt{\pi}} \sqrt{\pi \cdot 290^2 \cdot 0.013} = 66 \text{ nm} \quad (\text{approximation, confocal})$$

and

$$d \approx \frac{2}{\sqrt{\pi}} \sqrt{\pi \cdot 150^2 \cdot 0.12} = 104 \text{ nm} \quad (\text{approximation, STED}).$$

5. Discussion

Sizing of the 40 nm NPs using siFCS analysis and a confocal microscope of 270 nm FWHM was possible despite the presence of gaps between NPs. If the gaps had been smaller the sizing would have been even more accurate. Accordingly, if gap-free samples can be prepared, for example by fluorescence labeling of the phospholipids in bilayers or cells, it should be possible to determine the size of domains smaller than 40 nm even when using a diffraction-limited confocal microscope.

This is also the indication when comparing with previous iFCS analyses. In the first demonstration of iFCS nanoparticles down to 93 nm diameter could be analyzed in a 0.3 fL detection focus, indicating that particles could be detected as long as the particle to detection volume-ratio was not smaller than about 1 to 600 [13]. Approximately the same 1 to 600 ratio was observed when iFCS was used to determine the volume of protein molecules to 250 nm³, which were the smallest particles that could be analyzed in nanowells using a detection volume of 1.2·10⁻⁴ fL [17]. If a 1 to 600 ratio can be reached on a surface then the size of

domains of 20 nm diameter can be determined using confocal imaging, and below 5 nm diameter using STED imaging.

Nanodomains and protein clusters occur in various sizes in membranes and the distribution of such sizes may be analyzed by intensity distribution analysis, which has been utilized previously for iFCS [17].

iFCS was here applied by scanning fixed surfaces made to resemble membranes consisting of green labeled phospholipids and red labeled domains/clusters. Super-resolution imaging of fixed cells is routinely performed using STED- and PALM/STORM-imaging. Standard STED microscopes have a resolution of about 40-50 nm [23] while examples of state of the art STED microscopes have been shown with a resolution of about 20 nm [24]. The localization techniques PALM/STORM can come down to a resolution of about 20 nm.

Since transmembrane proteins have a diameter of 2-3 nm, there is thus still a need for techniques that can determine the size of clusters and domains in the range 1-20 nm.

Furthermore, even though STED microscopy with a time resolution of 35 ms on a small area of a living cells has been achieved [8, 25], the super-resolution techniques are generally applied to fixed cells and cannot analyze fast dynamics. In contrast, parked-beam iFCS should be applicable to fluid membranes which should have significant advantages. Not only would perturbation of the living cell be avoided, it would allow the on-line addition/removal of substances and monitoring of their effect on the size of nanodomains.

6. Conclusions

We have demonstrated the application of siFCS on fixed surfaces to determine the absolute size of domains on the surface. Using a confocal microscope with a resolution of 270 nm FWHM, the projected area of fluorescent NPs with a specified diameter of 250 nm was estimated to 257 ± 12 nm, and the projected area of NPs with a specified diameter of 40 nm was estimated to 65 ± 26 nm (both values are from the cross-talk compensated images). The deviation of the latter estimate from the specified value relates to the mean distance, “gap”, between NPs on the surface. For the 40 nm NPs also STED imaging could be used for siFCS analysis, but was more sensitive to the presence of gaps between NPs.

Here immobile surfaces were analyzed using siFCS, but two-dimensional mobile surfaces such as lipid bilayers or living cell membranes should also be suitable targets, by instead using parked-beam iFCS. Such analysis can be performed either using a confocal or a STED-microscope, and should be able to determine the sizes of mobile domains, rafts and protein clusters below 10 nm diameter.

Acknowledgments

We thank Dr. Per Thyberg for discussions.